Available online at www.CivileJournal.org

Civil Engineering Journal

(E-ISSN: 2476-3055; ISSN: 2676-6957)

Vol. 12, No. 02, February, 2026

Effect of Dike Width on Pore Pressure and Water Content Evolution During Overtopping Conditions

Marwan A. Hassan [1*], Heyam H. Shaalan [2], Hayder A. O. Al-Deewan [1]

[1] Department of Civil Technologies, Southern Technical University, Basra, Iraq.

[2] Department of Oil and Gas Engineering, Basra University of Oil and Gas, Basra, Iraq.

Received 14 July 2025; Revised 27 December 2025; Accepted 04 January 2026; Published 01 February 2026

Abstract

The failure of dike embankments due to overtopping flow plays a crucial role in understanding the mechanisms behind dike erosion, which is essential for effective disaster mitigation. The "SLIDE" program was used to analyze the transient response of pore water pressure (PWP) and volumetric water content (VWC) within a homogeneous coarse sand bed. The authors have previously examined the use of seepage-control elements in 3D simulations of embankment breach failures due to overtopping, conducted in laboratory flumes at the University of Science of Malaysia. In this study, pore water pressure (PWP) and volumetric water content (VWC) were measured at various points beneath the crest and along both the upstream and downstream slopes for three different dike crest widths: 7 cm, 12 cm, and 18 cm. This paper also presents a factor of safety (FOS) analysis across the unsaturated–saturated zones within the dike embankment during the events of overtopping moments until full saturation of the downstream slope. The results indicate that increases in both PWP and VWC occurred across all test groups along the slopes. Narrower crest widths led to higher pore water pressure at the onset of overtopping, while wider crest widths resulted in increased pore pressure toward the end of the erosion process. A reduction in the factor of safety was observed along the crest and downstream slope. However, in dikes with wider crest widths, the length of the embankment decreased due to prolonged flow discharge through the downstream toe and remnants of the upstream slope. The transient flow and slope stability results provide new insights into the coupled hydromechanical behavior of dike soil during overtopping events.

Keywords: Dike; Overtopping; Pore Water Pressure; Volumetric Water Content; Factor of Safety.

1. Introduction

Dike embankments are cost-effective hydro-engineering structures designed to protect populations from natural disasters such as floods, support irrigation, water supply, and energy generation [1, 2]. Constructed using homogeneous or non-homogeneous earthfill materials, they are commonly referred to as embankment dams or fill-type dams [3, 4]. With rising sea levels and increasing peak river discharge due to climate change, dikes must be reinforced to ensure long-term stability and safety [5, 6]. The failure of dike embankments is a catastrophic event that poses significant threats to human life and property [7, 8]. Among the various failure mechanisms, overtopping is the most frequent worldwide, surpassing sliding and piping failures [9, 10]. The erosion of soil and sediment by flowing water is known as scour [11, 12]. Overtopping-induced floods are responsible for 20,000 deaths each year and affect over 20 million people globally [13]. In India, severe overtopping events—such as those in Uttarakhand (2013),

* Corresponding author: marwan.adil@stu.edu.iq

https://doi.org/10.28991/CEJ-2026-012-02-016

© 2026 by the authors. Licensee C.E.J, Tehran, Iran. This article is an open access article distributed under the terms and conditions of the Creative Commons Attribution (CC-BY) license (http://creativecommons.org/licenses/by/4.0/).

Chennai (2015), and Kerala (2018)—have resulted in thousands of deaths [14]. Several laboratory experiments have been conducted to investigate the seepage behavior of overtopping flows across porous boundaries, such as sand beds [15–18]. Different geometric parameters were evaluated for their influence on the behavior of cohesive dike materials such as dam slopes and crest width [19].

The findings indicated that these parameters have a noticeable effect on the rapid erosion of the dike at stage 1, whereas their influence becomes minimal during the second stage (gradual evolution toward the equilibrium state). Al-Riffai and Nistor emphasized the importance of analyzing breach outflow hydrographs using a series of 3D breach overtopping experimental models [20]. They stated that proper drainage at the downstream slope of the earthfill dike reduces the erosion process in the channel due to the infiltration. Furthermore, control compaction during the construction significantly affects erosion and side slope failure. Urbaniak et al. examined the behavior of the breach process for a homogeneous earth dike composed of non-cohesive materials. They classified the widening of breach failure into three distinct stages: the initiation phase, the vertical erosion phase, and the reservoir emptying phase [21]. They concluded that geometric parameters of dike breach depend on the amount of water storage in the upstream slope, rather than on the rate of breaching phenomenon. Koshiba et al. conducted breach experiments for a homogeneous levee composed of silica sand No. 7 and a composite levee consisting of silica sand No. 5 and No. 7 [22]. The results showed that the breach shape differed significantly between the homogeneous and composite levee. The rate of breach widening was faster in the composite materials, resulting in a large overflow rate. A series of 418 experimental tests were analyzed to investigate the dike behavior, comprising a 1:6:3 foreshore slope and three different dike slopes, under first-order wave generation theory [23].

The results indicate that overtopping volumes are influenced by the focus phase. The critical locations for breach channel initiation were found to be at a distance of one-third of the deep-water wavelength from the toe. Meer et al. conducted a series of tests on grass-covered dike slopes, introducing a geometrical transition from slope to berm and a smooth asphalt transition on a horizontal plane [24]. They emphasize that the flow velocity increases over the slope due to gravity, while the horizontal berm significantly reduces the velocity. The asphalt cover effectively terminated cliff erosion. Various numerical models have been developed to simulate dike erosion processes [25–27]. These models are typically based on depth-averaged flow models; however, flow behavior over dikes, especially at the crest and slope toe, is complex. To better capture these dynamics, vertical two-dimensional simulations based on the Lagrangian approach have been proposed, enabling the representation of fluid and sediment particle motion [28]. Additionally, the scour depth around rectangular spur dikes has been investigated using the Renormalization Group (RNG) turbulence model coupled with the van Rijn sediment transport model [29]. The results indicate that scour depth increases with higher bed load coefficients near the spur dike. Wu et al. analyzed the influence of soil porosity on hydraulic properties and soil erosion during overtopping failure using a sediment scour model with suspended load [30].

The findings revealed that denser materials delayed the breach duration and reduced the erosion process. Although porosity parameters didn't affect the duration of the breach process, they did influence the magnitude of peak flow. Chen et al. developed a two-dimensional vertical (2DV) numerical model using the OpenFOAM framework to simulate overtopping flow velocity and layer thickness at the waterside edge of the dike crest [31]. The model demonstrated good predictive capability for overtopping parameters, with only a slight overestimation of layer thickness and a low exceedance probability of 2%. In the present study, the responses of pore water pressure (PWP), volumetric water content (VWC), and factor of safety (FOS) were analyzed for three different dike crest widths using coarse sand material. The simulations used SLIDE software to evaluate the influence of overtopping on dike stability during transient flow towards the downstream slope. The dike geometry used in this simulation was consistent with that of the experimental tests [32].

2. Research Methodology

The experimental dike section was previously described by Hassan & Ismail (2018) [32]. In their study, various mechanical and hydraulic properties were investigated using tensiometers and Time Domain Reflectometry (TDR) sensors. The experimental measurements related to the earthen embankment profile under overtopping conditions were conducted at the Hydraulic Laboratory of Universiti Sains Malaysia. The tensiometer and Time Domain Reflectometer (TDR) sensors were used to measure pore water pressure (PWP) and volumetric water content (VWC), respectively. They were distributed into six groups: A, B, C, D, E, and F, each consisting of one tensiometer and one TDR. Groups F and E were installed at the toe and mid-sections of the upstream slope; Group D was placed below the dike crest, and Group C was located at the transition area between the downstream and upstream slopes. Groups A and B were positioned near the toe and upper part of the downstream slope, respectively, as shown in Figure 1. The geometries of these slopes remained constant throughout the overtopping tests. In the current study, SLIDE software was employed to analyze the influence of embankment crest width on dike stability during overtopping flow. To assess the dike stability problem, the pore water pressure (PWP) was evaluated based on the Soil Water Characteristics Curve (SWCC) and hydraulic conductivity functions. The Soil Water Characteristics Curve (SWCC) represents the

relationship between the matric suction and the volumetric water content and can be determined experimentally or estimated using empirical methods for unsaturated soil [33].

The negative pore water pressure (PWP) or matric suction in unsaturated soil develops due to atmospheric pressure with two stresses of effective normal stress $\sigma' = (\sigma - u_w)$ and matric suction $\psi = (u_w - u_a)$, where σ, σ', u_w, and u_a represent the total normal stress, effective stress, pore water pressure and pore air pressure, respectively [34]. The matric suction is therefore considered a stress-state variable that governs the engineering properties for unsaturated soil. Based on the existence of air and water, the mechanical behavior of unsaturated soil is more complex than that of saturated soil. The phreatic surface, where pore-water pressure equals zero, divides the saturated and unsaturated zones. The unsaturated zone (vadose zone) may range from shallow (less than 1 m) to very deep (extending hundreds of meters or more) depending on the water table level. This zone is typically divided into three subzones based on the continuity of the air and water phases, as shown in Figure 2. The soil within the capillary fringe zone still contains a high degree of saturation, with negative pore water pressure relative to atmospheric conditions. The thickness of this zone ranges from 1 m to 10 m. In the second fluid phase, air penetrates the soil pores, while the water content remains relatively high, near or below the field capacity. In the final zone, the effect of atmospheric pressure leads to a dry state condition of the soil, while matric suction is generated inside the soil. Two of the most important engineering behaviors of soil are desaturation and saturation. In this study, laboratory test results were used as input parameters to estimate pore pressure, volumetric water content, and factor of safety (FOS), as illustrated in Figure 3. Based on prototype scaling, the coarse sand used in the experiments exhibited the typical behavior of non-cohesive materials, as shown in Figure 4.

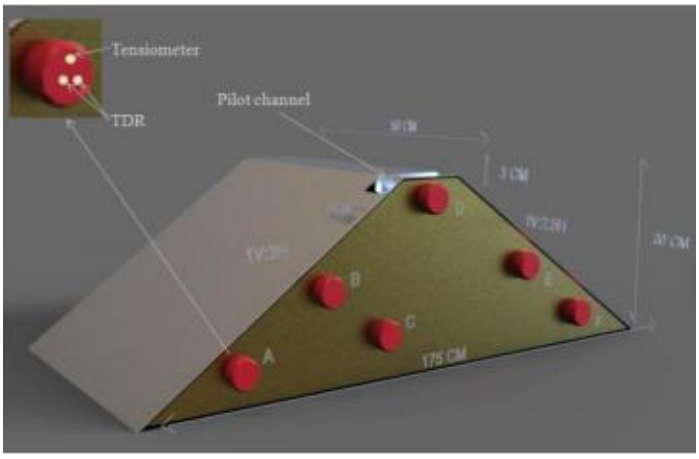

Figure 1. Locations of water sensors along the upstream and downstream slopes

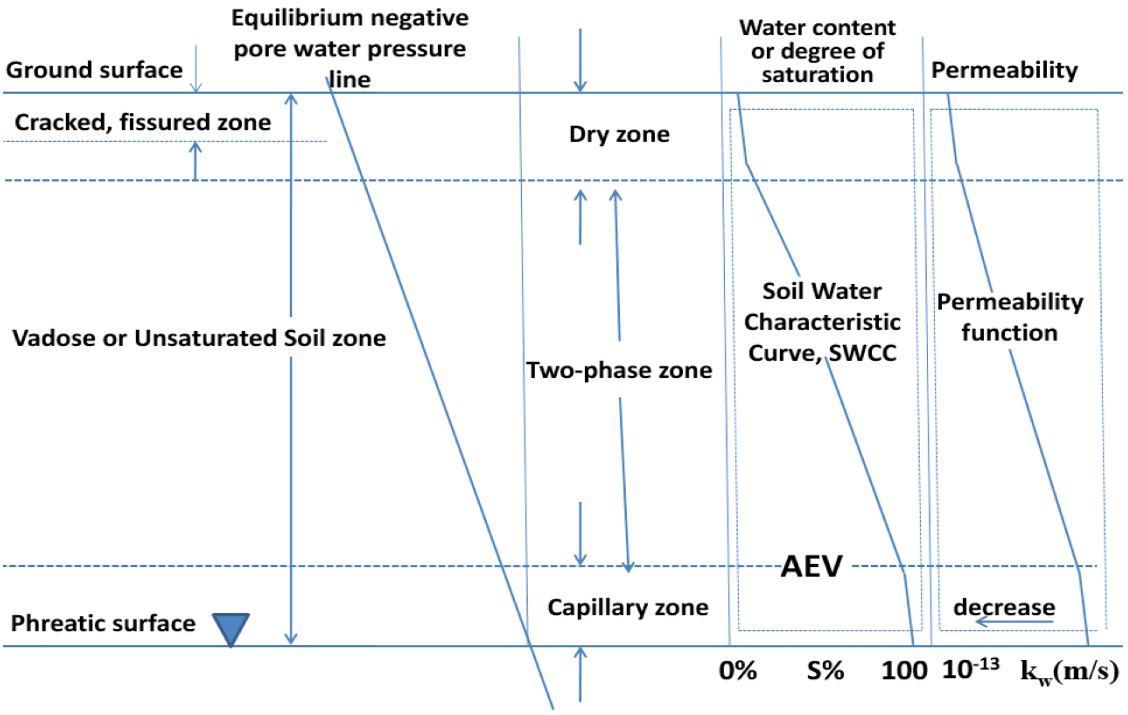

Figure 2. Classification of the vadose zones with unsaturated soil

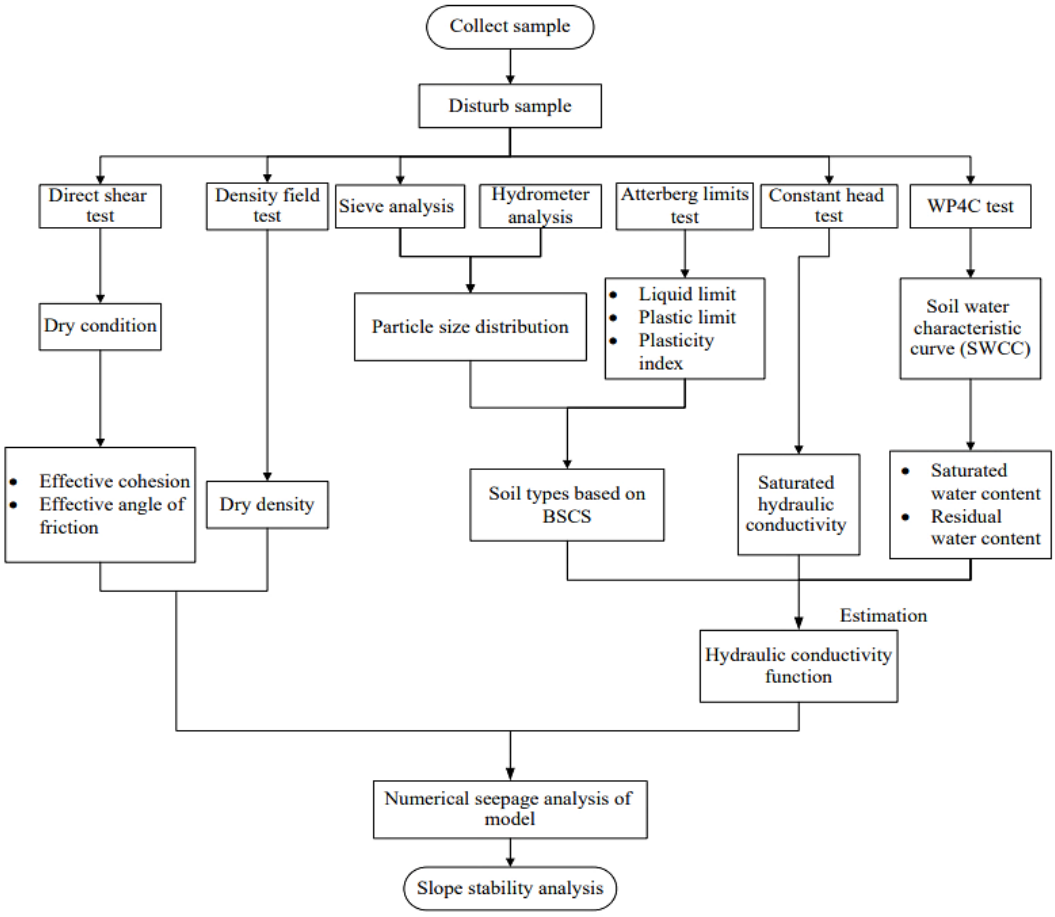

Figure 3. Flowchart for the input of soil properties

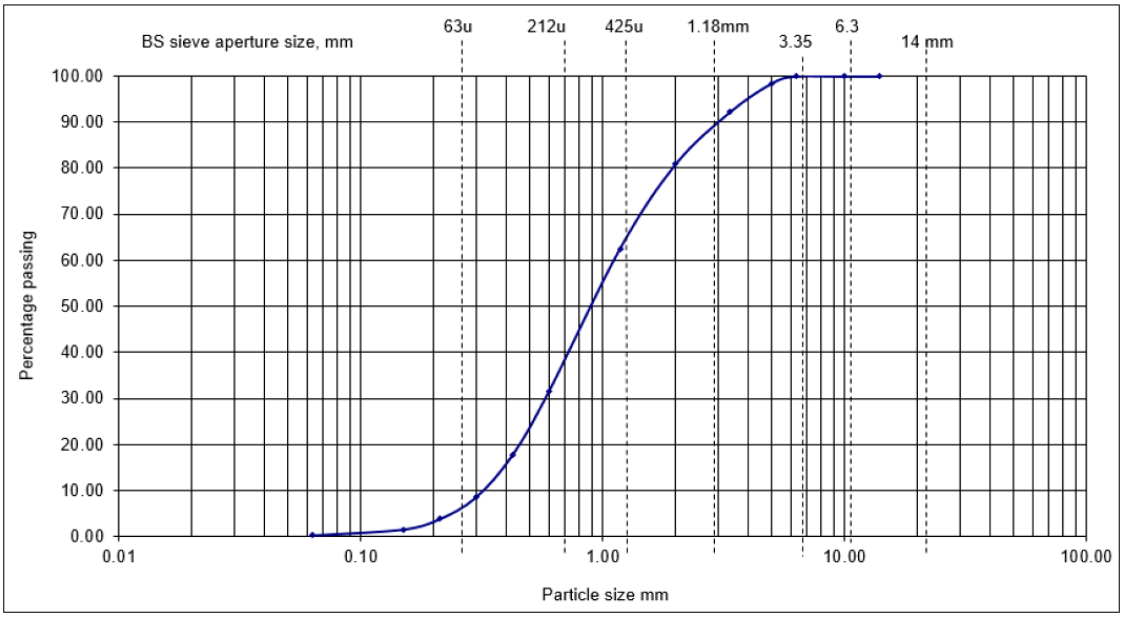

Figure 4. Grain size distribution of Coarse sand

The SLIDE program is a finite element-based software tool designed to analyze groundwater seepage and the dissipation of excess pore-water pressure within permeable materials such as soil and rock. It utilizes input parameters, including the volumetric water content and hydraulic conductivity functions, to simulate the pore pressure response under overtopping flow conditions. In this study, particular attention was given to deriving the Soil Water Characteristic Curve (SWCC) for coarse sand. This was achieved using a Dew Point Potentiometer (WP4C) in combination with the Van Genuchten model to accurately characterize the hydraulic behavior of the soil. The Dew

Point Potentiometer (WP4C) is considered one of the most accurate, rapid, and reliable laboratory instruments for measuring the soil water potential (matric and osmotic). It is based on the chilled mirror system and measures the matric suction in the range of 0 to 300 MPa, with an accuracy of ± 0.05 MPa for suction values between 0 and 5 MPa for different types of soils. The measurement process involves equilibrating the water phase of the soil sample with the water vapor phase in a closed chamber, allowing the vapor pressure in the headspace to be determined. The WP4C consists of a sensor block, where the soil sample is placed, a dew point sensor, a temperature sensor, and an infrared thermometer. The dew point sensor determines the dew point temperature of the air, while a small fan accelerates the equilibrium process and monitors the boundary layer conductance of the dew point sensor. From these measurements, the water potential and temperature of the sample are obtained once equilibrium is achieved between the sample's water potential and the vapor air pressure in the headspace chamber.

$$\theta_n = \left[\frac{1}{1+(\alpha_\psi \psi)^{\eta_\psi}}\right]^{m_\psi} \quad (1)$$

In the Van Genuchten model, the parameters α_ψ, η_ψ, and m_ψ represent the air-entry value (AEV), the slope line of SWCC curve and the residual water content, respectively. On the other hand, The Fredlund and Xing model assumes that the pore size distribution influence the shape of Soil Water Characteristics Curve (SWCC) through a correction factor $C(\psi)$.

$$\theta_w = C(\psi)\frac{\theta_s}{\left\{ln\left[e+\left(\frac{\psi}{\alpha_\psi}\right)\right]^{\eta_\psi}\right\}^{m_\psi}} \quad (2)$$

Here, e denotes the base of the natural logarithm, and α_ψ, n and m are curve fitting parameters. The Van Genuchten equation provides greater flexibility in representing Soil Water Characteristics Curve (SWCC) and covers a wide range of matric suction for different types of soil due to the inclusion of parameter m, which provides more stability during optimization. The relationship is often simplified by setting m = 1-1/n ($n > 1$, $0 < m < 1$) to establish a constant m and to provide a closed- form expression. The input parameters used for estimating the volumetric water content function and the hydraulic conductivity function of the coarse sand are presented in Tables 1 and 2, respectively. Once the volumetric water content function is determined, the hydraulic conductivity function can be derived accordingly.

Table 1. Parameters of volumetric water content function

Dike widths	Source of input parameter	Parameters of volumetric content function		Curve fitting parameters		
7	WP4C test and Data function built in SLIDE	Saturated water content (%)	Residual water content (%)	a	n	m
12						
18		19	1	15.1	7.35	0.86

Table 2. Parameters of hydraulic conductivity function

Dike widths	Parameters of hydraulic conductivity function			Curve fitting parameters		
7	Saturated water content (%)	Residual water content (%)	Saturated hydraulic conductivity	a	n	m
12						
18	19	1	1×10^{-3}	15.1	7.35	0.86

Limit Equilibrium Method (LEM) is considered one of the earliest methods to study the slope stability. It estimates the minimum and most critical Factor of Safety (FOS) value using applied stress and mobilized strength in the slope over a trial slip surface. The shape of the slip surface differs significantly for different methods of limit equilibrium, such as circular, planar, logarithmic, etc., analysis. FOS is evaluated based on the relationship between the anti-sliding force and the sliding force [35]. Other numerical models have also been developed to calculate FOS, such as Slip Surface Stress Analysis (SSA) and Strength Reduction Method (SRM). Similar to LEM, the SSA method estimates FOS based on the principle of surface weight average. The SRM, on the other hand, is simpler than SSA and widely implemented in numerical software. It determines FOS by progressively reducing shear strength parameters until slope stability failure occurs. In this study, the slope stability analysis was performed using the General Limit Equilibrium (GLE) method. This approach evaluates the factor of safety (FOS) based on both moment equilibrium and horizontal force equilibrium. It can be applied to both circular and non-circular failure surfaces and considers both interslice normal and shear forces. The FOS equation derived from moment equilibrium can be expressed as follows:

$$Fs_m = \frac{\sum(c'\beta R+(N-u\beta)R\tan\theta')}{\sum Wx-\sum Nf} \quad (3)$$

$$Fs_f = \frac{\sum(c'\beta\cos\alpha+(N-u\beta)\tan\theta'\cos\alpha)}{\sum(N\sin\alpha)} \quad (4)$$

where, W = Total weight of slice; P = Total normal force on slice base; s_m = shear force acting on the base on slice; R = moment arm related to with the shear force s_m; f= perpendicular offset of the normal force from the centre of rotation; x = Horizontal distance from the slice to the center of rotation; β = Base length of each slice; α = Angle between the tangent to the center of the base of each slice and the horizontal; c' = effective cohesion; $\emptyset'$ = Effective angle of friction; u = pore water pressure; Fs_m = Factor of safety of moment equilibrium; Fs_f = Factor of safety of force equilibrium.

The terms H1, H2, and H3 refer to the numerical analysis of transient seepage and slope stability for dike crest widths of 7 cm, 12 cm, and 18 cm, respectively.

2.1. Numerical Analysis of Water Content and FOS

The transient seepage simulation was modeled by defining a homogeneous soil domain composed of coarse sand, as illustrated in Figure 5. Material properties such as cohesion, saturated hydraulic conductivity, and angle of internal friction were specified for three different crest widths (7 cm, 12 cm, and 18 cm), as detailed in Table 3. A constant head of 30 cm—corresponding to the dike height—was applied along the upstream slope to define the seepage boundary conditions for the transient flow analysis. In addition, soil parameters, including the grain size distribution and saturated water content, were required to predict the Soil Water Characteristic Curve (SWCC) and hydraulic conductivity function. The simulation began by applying water flow at the toe of the upstream slope, where the pore water pressure (PWP) was initially set to zero at all sensor locations. The model was then discretized into a finite element mesh. SLIDE 2018 subsequently computed the pore water pressure and volumetric water content at each sensor within the finite element mesh throughout the progression of flow towards the downstream slope.

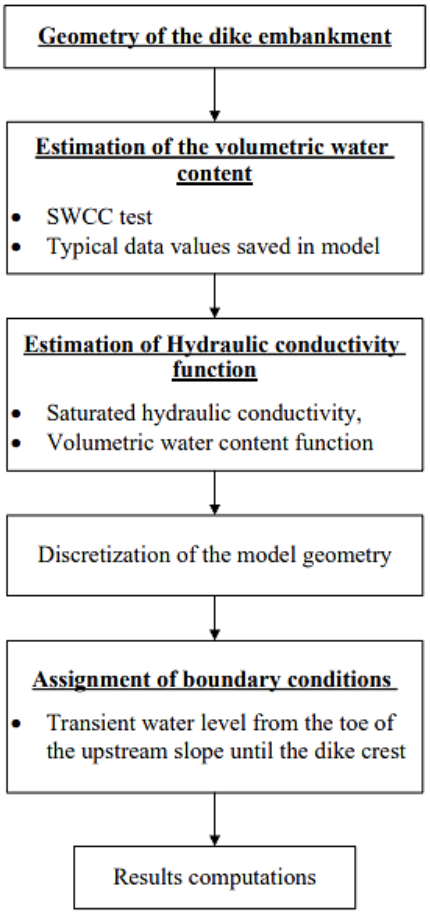

Figure 5. Steps involved in the transient seepage analysis

Table 3. Soil properties of coarse sand

Input parameters	Values
Gravel (%)	19.1
Sand (%)	80.59
Silt (%)	0.31
Clay (%)	0
Soil classification using BSCS	SP
Dry unit weight (kN/m³)	18
Hydraulic conductivity (m/s)	1×10^{-3}
Effective cohesion (kPa)	0
Effective angle of friction (°)	37
Saturated water content (m³/m³)	0.19
Residual water content (m³/m³)	0.01

The numerical simulations also proved valuable by providing insights into the calculation of the factor of safety (FOS) during the erosion process of the dike embankment using the GLE method, as illustrated in Figure 6. The total duration for the transient water flow and slope stability analysis was set to 600 seconds. At the end of transient analysis, the General Limit Equilibrium method (GLE) generated a single FOS value for the entire slope, where FOS calculated from moment equilibrium (Equation 3) and force equilibrium (Equation 4) are equal when both equations are satisfied. Based on these simulations, the effects of the three different dike crest widths were plotted, revealing the corresponding seepage behavior for each crest configuration.

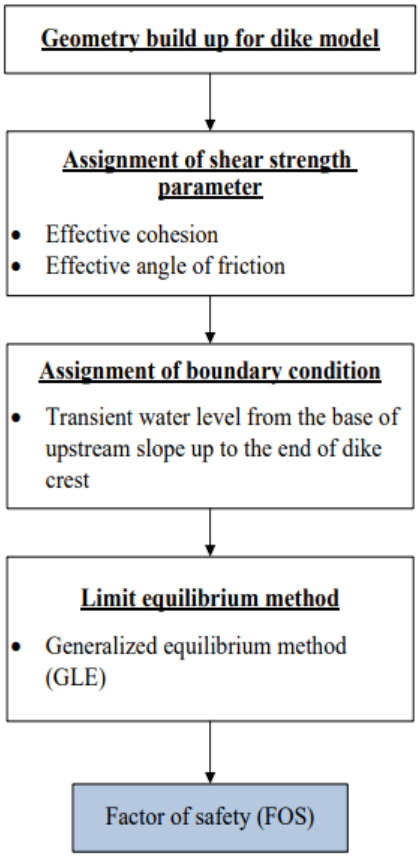

Figure 6. Schematic diagram of the dike slope stability analysis

3. Results and Discussion

Three dike crest widths of 7 cm, 12 cm, and 18 cm (denoted as H1, H2, and H3, respectively) were used in the numerical modeling. The pore water pressures (PWP) and the time of transient flow from the upstream to downstream slopes were plotted on the Y-axis and X-axis, respectively. The downstream slope had a vertical-to-horizontal ratio of 1V:3H, while the upstream slope was 1V:2.5H, representing the geometry of the main dam structure. The

embankment was modeled using pure coarse sand, consistent with the experimental tests. Figures 7 to 12 illustrate the development of pore water pressures across sensor groups A, B, C, D, E, and F. At the start of the simulation (t = 0 seconds), the bottom layer of the sand embankment was saturated due to the presence of water flow within the soil pores. Water infiltration at the toe of the upstream slope was initially minor owing to the high matric suction in the dry soil, which contributed to the dike's stability. Over time, the unsaturated soil gradually became saturated as water content increased and negative pore water pressure decreased. The soil properties significantly influenced the degree of saturation. The sand particles were affected by their weight and frictional characteristics, which accelerated flow permeability. The large particle size of the coarse sand enhanced permeability due to the presence of water bound on the particles' surfaces. This bound water limited groundwater migration, particularly in pores smaller than twice the thickness of the adsorbed water layer. Both pore water pressure (PWP) and volumetric water content (VWC) increased across all sensor groups.

The results for groups E and F—located near the toe and mid-section of the upstream slope—were very similar, reflecting rapid saturation at the base of the embankment. The maximum recorded PWP and VWC were 2.25 kPa and 0.20, respectively, for group F. Vertical erosion initiated breach channel formation when the overflow reached the dike crest. As erosion extended to the toe of the downstream slope, the channel expanded longitudinally towards the center of the dike body. With further erosion of the lower part of the dike, the remaining mid- and upstream toe sections eventually collapsed. Consequently, the maximum PWP occurred near groups F and E at the end of the transient flow process compared with other groups. Groups A and B exhibited a faster increase in PWP than groups C and D. Notable changes in PWP occurred around t = 1400 seconds for groups A and B and at t = 1500 seconds for groups C and D. This difference was attributed to the steeper downstream slope, which accelerated saturation and erosion processes, particularly in the mid and toe regions. The breach failure was more pronounced in the downstream slope than at the crest and upstream sections. This was because the downstream slope was more exposed to out-of-bank forces and required a longer time for the breach channel to reach a steady-state condition (equilibrium). The figures also demonstrated that the shorter dike crests (H1 and H2) produced higher PWP values than H3 at t = 1400 seconds, after which erosion failure reached an equilibrium state.

Meanwhile, the saturation process continued longer for H3 at t = 2000 seconds. The shorter dike crest generated greater discharge through the breach channel compared with the wider crest. For groups C and D, the PWP values were similar for all dike crest widths at t = 2000 seconds. As the dike collapsed, the water flow volume increased rapidly below the crest, while the downstream water depth decreased accordingly. The results showed good agreement with the findings of Duan et al. [36]. Who reported that the pore water pressure rose slowly in the occasional tailing pond, tended to stabilize, and then rapidly decreased during the overtopping flow? In our case, although the numerical modeling did not progress into a clear post-failure drop of pore pressure, the gradual transitions from matric suctions to positive pore water pressure, along with the plateauing phase at the end of the erosion process, were consistent with the mechanism of dike failure under overtopping conditions.

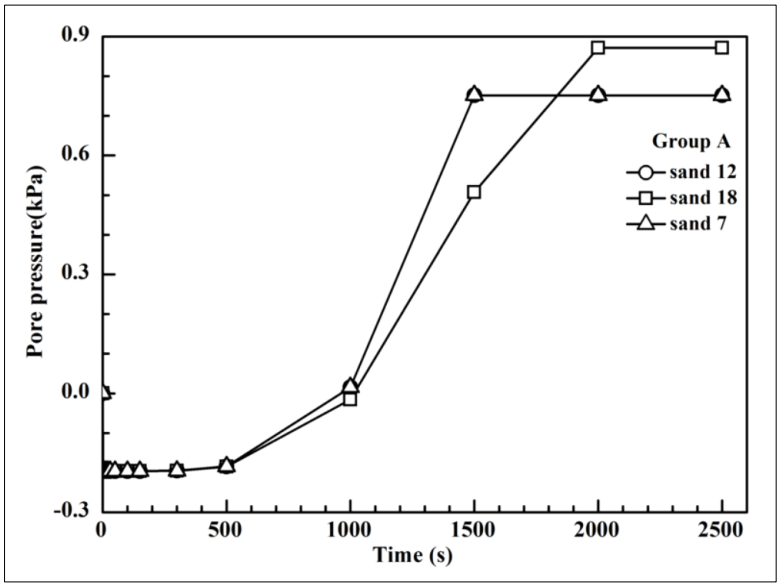

Figure 7. Development of pore water pressure (PWP) over time for sensor group A

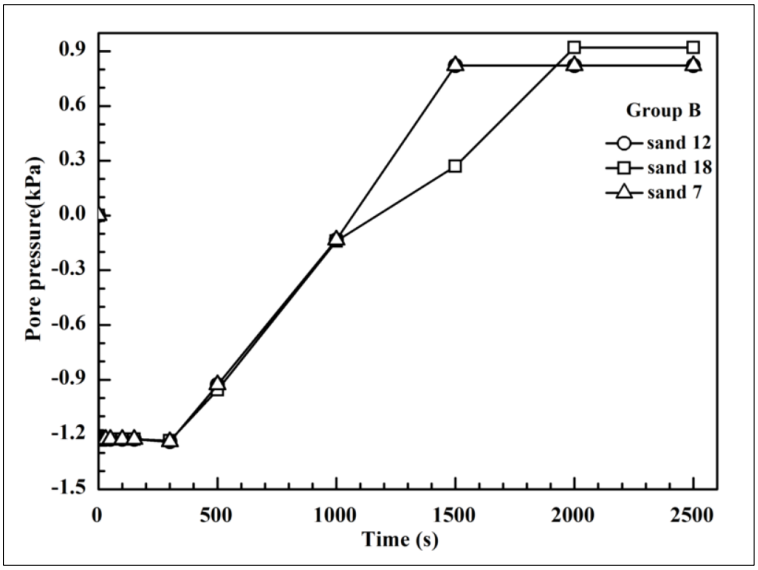

Figure 8. Development of pore water pressure (PWP) over time for sensor group B

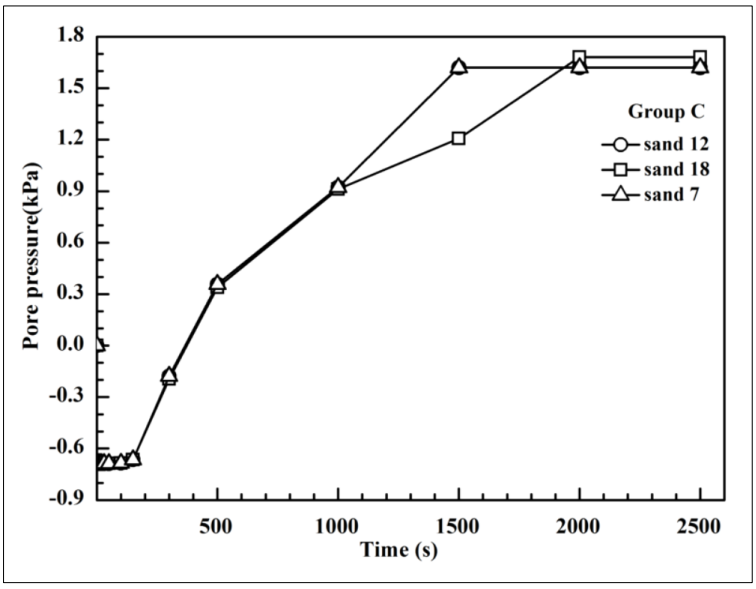

Figure 9. Development of pore water pressure (PWP) over time for sensor group C

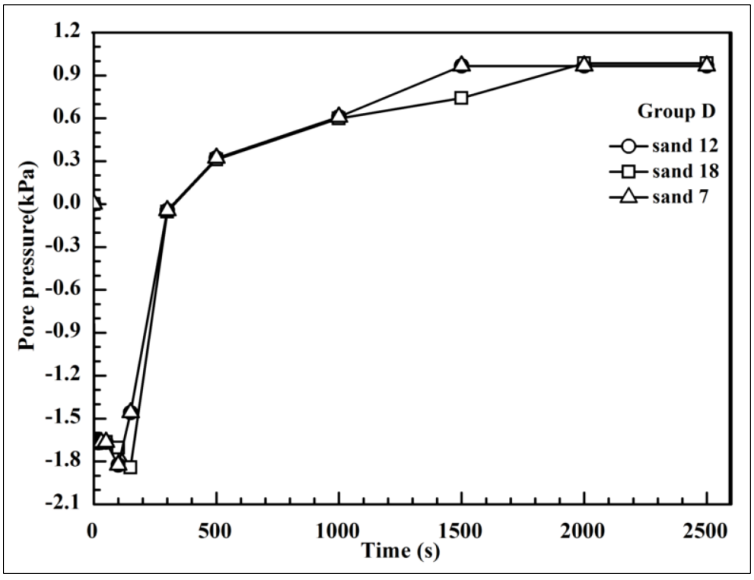

Figure 10. Development of pore water pressure (PWP) over time for sensor group D

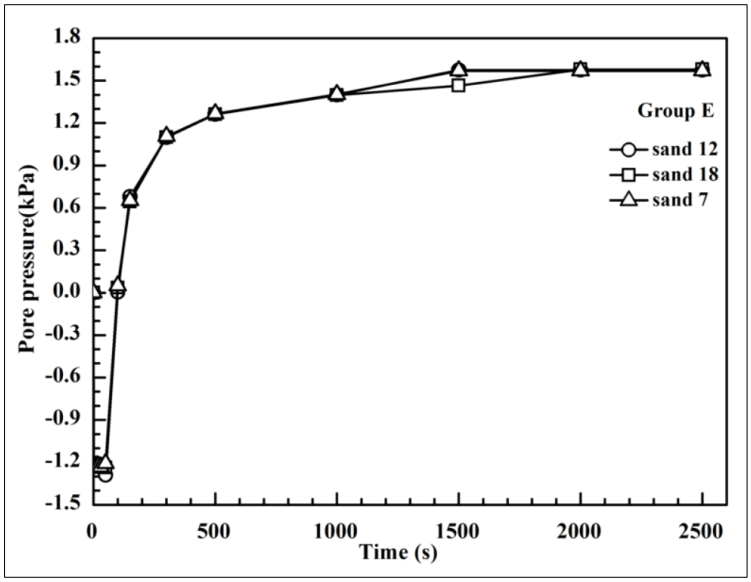

Figure 11. Development of pore water pressure (PWP) over time for sensor group E

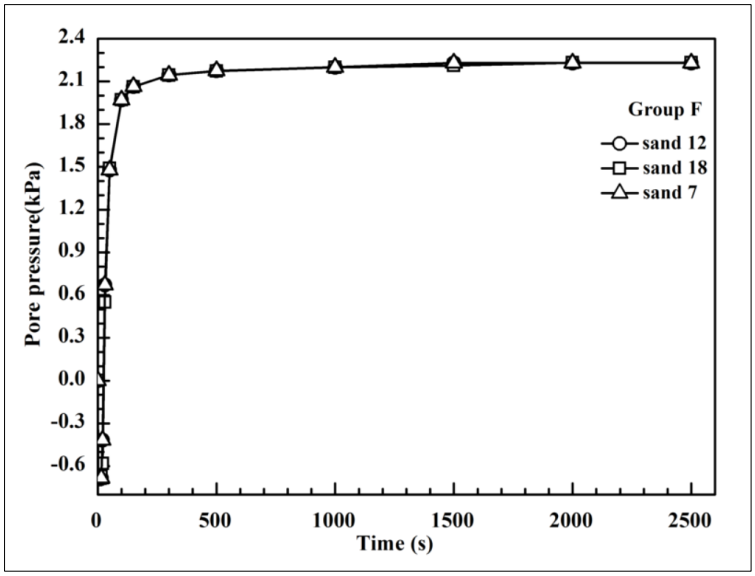

Figure 12. Development of pore water pressure (PWP) over time for sensor group F

Figures 13 to 18 illustrate the evolution of volumetric water content (VWC) for the three dike crest widths across sensor groups A, B, C, D, E, and F, respectively. The VWC was plotted on the Y-axis against the transient flow time from the upstream to downstream slopes on the X-axis. At the onset of water infiltration at the toe of the upstream slope, the dry sand embankment exhibited minimal tensile strength. As the water table gradually rose towards the midsection of the upstream slope, group E experienced the saturation of large unsaturated zones, resulting in higher pore water pressure (PWP) for crest widths H1 and H2 compared to H3 at t = 1500 seconds. Subsequently, an overtopping simulation was conducted, leading to a rise in the water table at the top of the upstream slope.

Tensile strength initially increased to a maximum as the degree of saturation progressively rose, governed by particle size and porosity, but later decreased to nearly zero at full saturation. A slight increase in pore water pressure within the air phase was observed at H1 and H2 after 1500 seconds in group D. This phenomenon occurred as water flowed over the dike crest and air pressure built up due to the disconnection of closed unsaturated pores from the atmosphere, caused by a thin surface of water layer combined with near-saturated sand at the surface. At Group A, PWP was higher for H1 and H2 at 1000 seconds, whereas H3 exhibited a higher value at 2000 seconds. Similarly, VWC was higher for H1 and H2 at 500 seconds. Continued infiltration submerged the unsaturated zone in the downstream slope, reduced the unsaturated soil volume, and caused noticeable pressure increases in groups A and B.

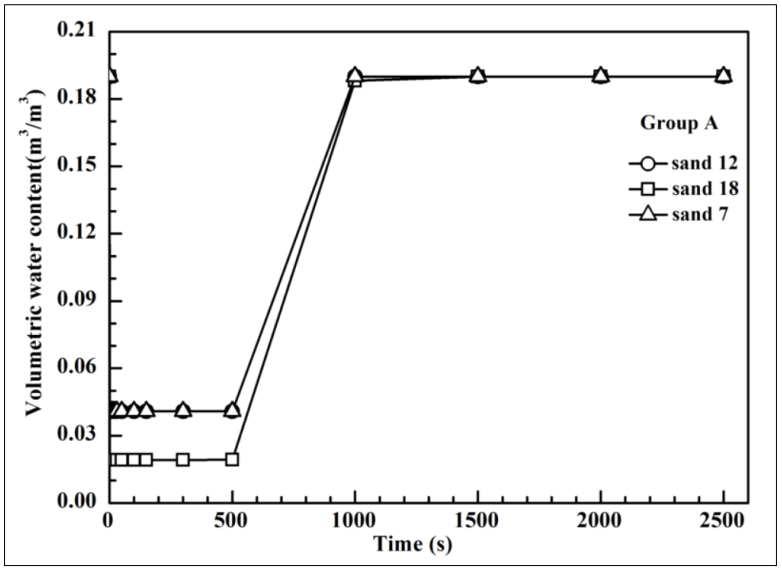

Figure 13. Development Volumetric water content (VWC) over time for sensor group A

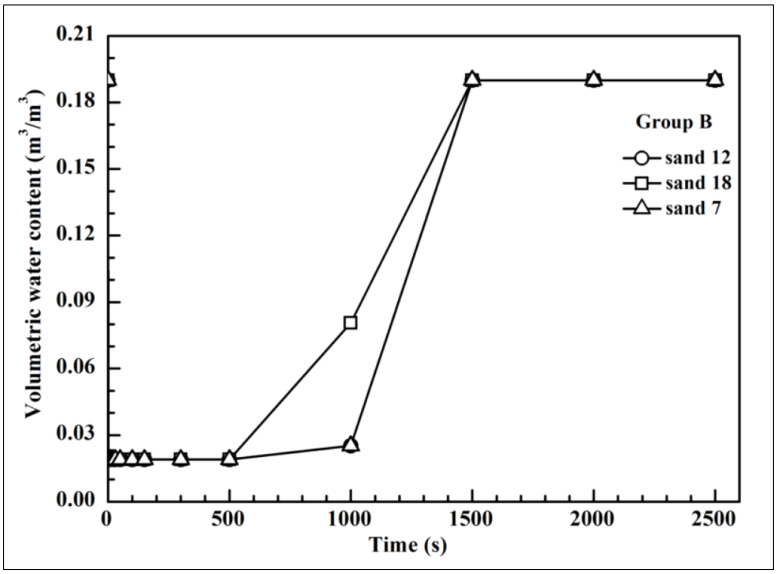

Figure 14. Development Volumetric water content (VWC) over time for sensor group B

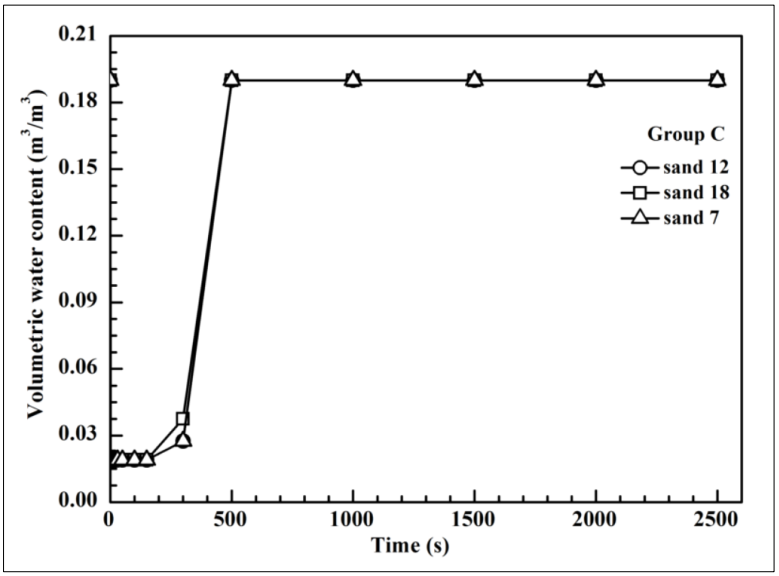

Figure 15. Development Volumetric water content (VWC) over time for sensor group C

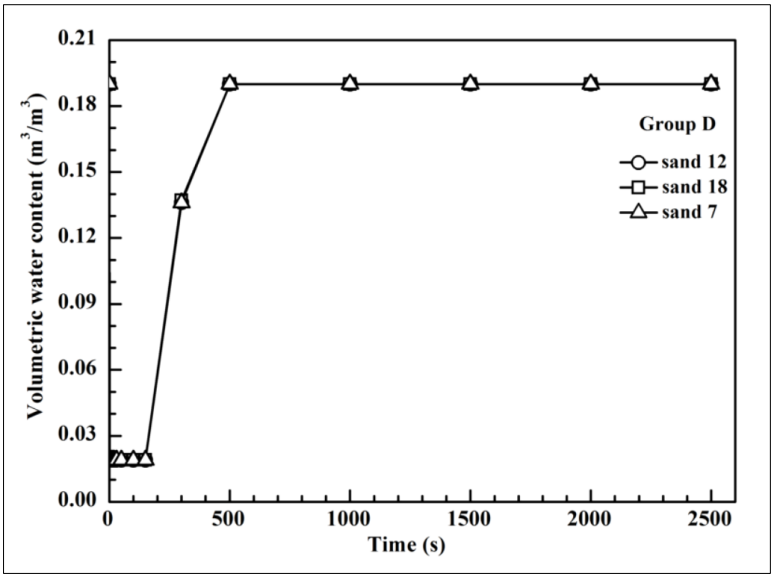

Figure 16. Development Volumetric water content (VWC) over time for sensor group D

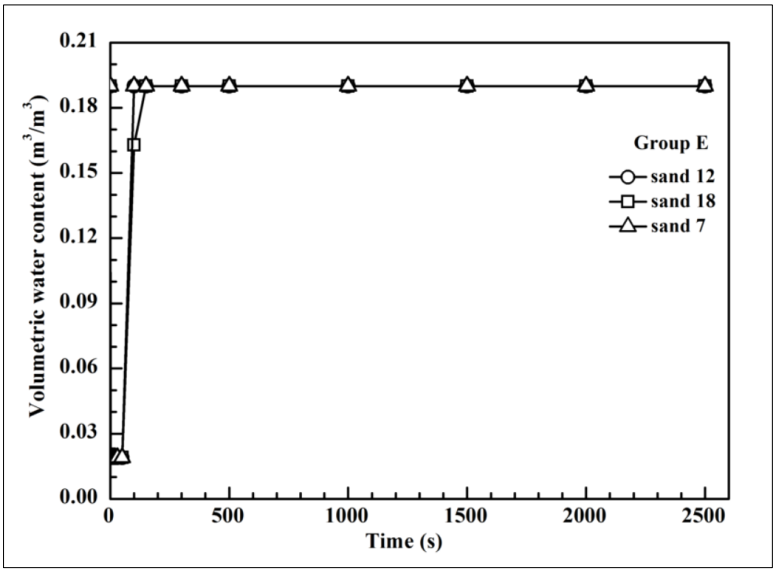

Figure 17. Development Volumetric water content (VWC) over time for sensor group E

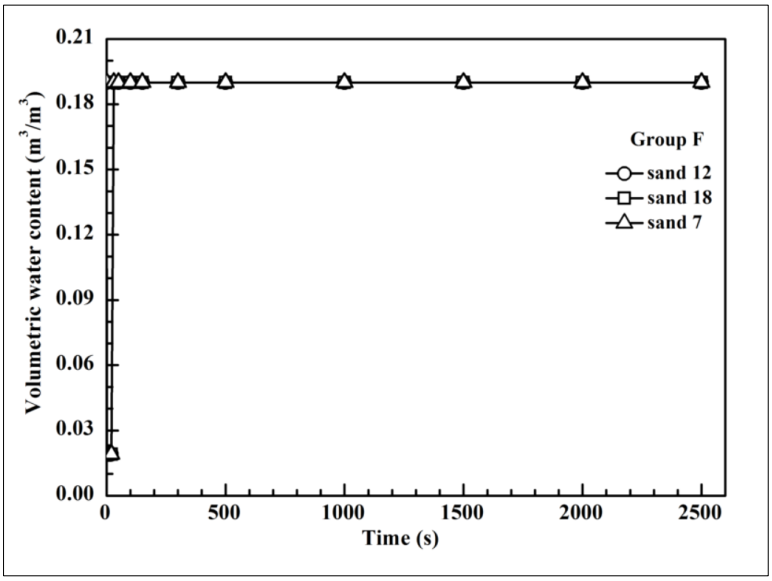

Figure 18. Development Volumetric water content (VWC) over time for sensor group F

The volume of void at the interface between saturated and unsaturated zones expanded as entrapped air zones diminished. The maximum PWP occurred at t=1500 seconds for H1 and H2 and at t = 2000 seconds for H3. This peak corresponded to the formation of narrow cracks within thin saturated layers along the outer dike slope. Subsequently, PWP decreased as air escaped through cracks that developed in both the upper and lower portions of the downstream slope. The greatest instability of the downstream slope was observed at the onset of overtopping and persisted even after a slight reduction in pore pressure. Meanwhile, the thickness of eroded material downstream of the original dike continued to increase. For Group B, the volumetric water content (VWC) was higher for H3 at 1000 seconds, due to the continuous void saturation and faster material loss in the upper and middle portions of the downstream slope. Eventually, PWP values stabilized as erosion slowed and the dike surface approached a near-horizontal profile. Overall, the numerical results indicated that test duration increased with crest widths, primarily due to the larger void volume within the dike body.

In this study, the General Limit Equilibrium (GLE) model was used to examine the inverse linear relationship between the crest widths and the initial factor of safety. The FOS is plotted on the Y-axis against the transient flow time from the upstream to downstream slopes on the X-axis. Figure 19 compares the variation in FOS for the three dike crest widths. A reduction in FOS occurred during the transition of water flow from the upstream slope towards the downstream slope. When the water flow reached the crest, the energy gradient and flow velocity were initially low, resulting in small tractive stress and limited erosion. However, erosion intensified along the downstream edge of the crest due to higher tractive stresses and increased flow velocity. This process reduced the crest width and, consequently, the embankment height. The general trend of FOS degradation was consistent across all crest widths. At the onset of overtopping, the flow depth above the crest was low, and the erosion started at the front edge of the embankment crest. Therefore, no significant erosion or degradation occurred in the upstream portion of the embankment. At t = 0 seconds, FOS values were 2.47, 2.35, and 2.15 for H1, H2, and H3, respectively. The higher FOS values observed for narrower crests (H1 and H2) are attributed to the distribution of vertical normal stress resulting from the dike's self-weight over surface failure. This stress enhanced soil shear resistance, particularly in the absence of positive pore water pressure.

The reduction in FOS occurred more rapidly for H1 and H2 at t = 1400 seconds compared to H3. Greater water storage within the upstream slope accelerated the reduction of FOS for narrower crests due to increased soil saturation and pore pressure buildup. As the crest width increased, the overtopping flow path was lengthened, which led to a higher hydraulic head loss and a larger pressure drop along the seepage path. Consequently, the resistance to flow increased and the seepage rate decreased. These results were in agreement with findings of Verwaest et al. (2011), who reported that overtopping flow crossing over a coastal dike decreased significantly with increasing crest width. A wider width—of a few meters—reduced or dissipated the flow kinetic energy of the overtopping wave (breach discharge) over the crest, allowing parts of the flow to return towards the seaside [37]. As the upstream water level rose, both the peak flow and flow discharge at the crest and downstream slope increased, accelerating erosion and reducing slope stability. The breach channel first widened near the crest and toe sections and then extended through the middle of the dike body, ultimately leading to complete failure. By the end of the erosion process, hydraulic forces and energy slope decreased, causing flow velocity and erosion rates at the downstream toe to diminish. Erosion rates stabilized around t = 1500 seconds for H1 and H2 and at *t* = 2000 seconds for H3 due to the prolonged erosion process along the downstream slope.

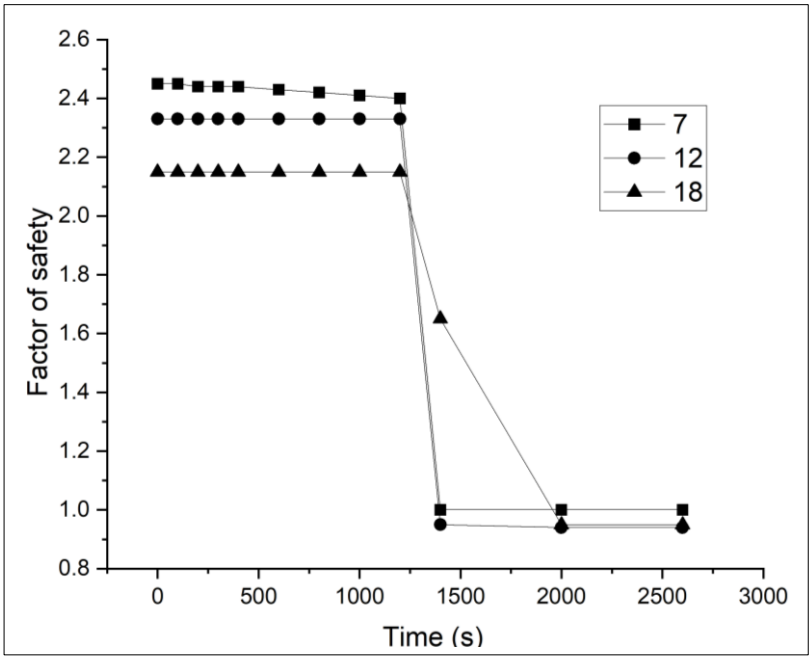

Figure 19. Development of the factor of safety (FOS) over time during the slope stability analysis

4. Conclusion

Embankment dikes play a vital role in protecting human safety, supporting infrastructure, generating power, and ensuring water supply. Understanding the geotechnical and hydraulic behavior of dikes under extreme loading conditions such as overtopping waves is essential for improving risk assessment and enhancing structural resilience. This paper presents a detailed numerical analysis for a homogeneous sand embankment subjected to flood overtopping using SLIDE software. The geometric configuration and material properties of the dike were previously established through laboratory experiments to ensure a realistic simulation of transient seepage flow. Three crest widths—7 cm, 12 cm, and 18 cm—were examined using six sensor groups (A, B, C, D, E, and F) distributed along the upstream and downstream slopes. For each sensor group, pore water pressure and volumetric water content were measured throughout the dike body. Additionally, the factor of safety (FOS) was evaluated using the General Limit Equilibrium (GLE) method to assess the slope stability under varying crest widths. For all groups of sensors, the PWP increased during the transient flow towards the downstream slope, primarily due to the reduction in matric suction within soil particles. At the onset of water infiltration, pore water pressure was higher for the 7 cm and 12 cm due to more rapid soil saturation and quicker dissipation of entrapped air. In contrast, the 18 cm crest exhibited higher pore pressure toward the later stages of the erosion process as a result of continued soil loss along the downstream slope. A reduction in FOS was observed for all crest widths, with the erosion process persisting longer for the wider crest due to extended erosion at the toes of both the downstream and upstream slopes.

5. Declarations

5.1. Author Contributions

Conceptualization, M.A., H.H., and H.A.; methodology, M.A., H.H., and H.A.; software, M.A.; validation, M.A., H.H., and H.A.; formal analysis, M.A.; investigation, M.A.; resources, M.A., H.H., and H.A.; data curation, M.A., H.H., and H.A.; writing—original draft preparation, M.A.; writing—review and editing, M.A. All authors have read and agreed to the published version of the manuscript.

5.2. Data Availability Statement

The data presented in this study are available on request from the corresponding author.

5.3. Funding and Acknowledgments

This work was partially supported by Southern Technical University under Scientific Research Award No. 9/7934, dated September 10, 2005.

5.4. Conflicts of Interest

The authors declare no conflict of interest.

6. References

[1] Wan Ariffin, W. N. H., Sidek, L. M., Basri, H., Idros, N., Adrian, M. T., Ghani, N. H. A., Khambali, H. M., Omar, S. M. A., Khebir, M. I. A., & Ahmed, A. N. (2025). Overtopping risk of high-hazard embankment dam under climate change condition. PLoS ONE, 20(2), 0311181. doi:10.1371/journal.pone.0311181.

[2] Gebremariam, F. T., Tesfay, A. H., Sigtryggsdóttir, F. G., Goitom, H., & Lia, L. (2025). Overtopping-Induced Embankment Breaching Experiments: State-of-the-Art Review on Measurement and Instrumentation. Water (Switzerland), 17(7), 1051. doi:10.3390/w17071051.

[3] Athani, S. S., Shivamanth, Solanki, C. H., & Dodagoudar, G. R. (2015). Seepage and Stability Analyses of Earth Dam Using Finite Element Method. Aquatic Procedia, 4, 876–883. doi:10.1016/j.aqpro.2015.02.110.

[4] Ahmed, S., Emmanuel, F., & Nyong Wilson, U. (2023). Finite Element Method of Seepage and Stability Analysis of Saura-Keffi Earth Dam. Malaysian Journal of Civil Engineering, 35(1), 53–61. doi:10.11113/mjce.v35.19591.

[5] van Bergeijk, V. M., Verdonk, V. A., Warmink, J. J., & Hulscher, S. J. M. H. (2021). The cross-dike failure probability by wave overtopping over grass-covered and damaged dikes. Water (Switzerland), 13(5), 1–22. doi:10.3390/w13050690.

[6] Jin, Y., Wang, W., Kamath, A., & Bihs, H. (2022). Numerical Investigation on Wave-Overtopping at a Double-Dike Defence Structure in Response to Climate Change-Induced Sea Level Rise. Fluids, 7(9), 295. doi:10.3390/fluids7090295.

[7] Graziano, A. A., Halso, M. C., Boes, R. M., Macchione, F., & Vetsch, D. F. (2025). Flood hazard assessment due to dam breaching considering river morphodynamics. Natural Hazards, 121(18), 21633–21663. doi:10.1007/s11069-025-07658-6.

[8] Ionescu, C. S., Gogoașe-Nistoran, D. E., Baciu, C. A., Cozma, A., Motovilnic, I., & Brașovanu, L. (2025). The Impact of a Clay-Core Embankment Dam Break on the Flood Wave Characteristics. Hydrology, 12(3), 56. doi:10.3390/hydrology12030056.

[9] Saberi, O., & Zenz, G. (2016). Numerical Investigation on 1D and 2D Embankment Dams Failure Due to Overtopping Flow. International Journal of Hydraulic Engineering, 2016(1), 9–18. doi:10.5923/J.IJHE.20160501.02.

[10] Zuo, Y. M., Zhou, J. W., Li, H. B., Zhang, J. Y., Tan, C., Wang, X. D., Wang, Y. S., & Zhou, Y. (2024). Overtopping Failure Process and Core Wall Fracture Mechanism of a New Concrete Core Wall Dam. KSCE Journal of Civil Engineering, 28(5), 1753–1766. doi:10.1007/s12205-024-0951-5.

[11] Omar, P. J., Gaur, S., & Dikshit, P. K. S. (2021). Conceptualization and development of multi-layered groundwater model in transient condition. Applied Water Science, 11(10), 162. doi:10.1007/s13201-021-01485-3.

[12] Gao, D., Pan, X., Liang, B., Yang, B., Wu, G., & Wang, Z. (2024). A Review and Design Principle of Fixed-Bottom Foundation Scour Protection Schemes for Offshore Wind Energy. Journal of Marine Science and Engineering, 12(4), 660. doi:10.3390/jmse12040660.

[13] Iqbal, S., & Tanaka, N. (2023). An Experimental Investigation on Dike Stabilization against Floods. Geosciences (Switzerland), 13(10), 1–19. doi:10.3390/geosciences13100307.

[14] Young, J. C., Arthur, R., Spruce, M., & Williams, H. T. P. (2022). Social sensing of flood impacts in India: A case study of Kerala 2018. International Journal of Disaster Risk Reduction, 74, 102908. doi:10.1016/j.ijdrr.2022.102908.

[15] Francalanci, S., Parker, G., & Solari, L. (2008). Effect of Seepage-Induced Nonhydrostatic Pressure Distribution on Bed-Load Transport and Bed Morphodynamics. Journal of Hydraulic Engineering, 134(4), 378–389. doi:10.1061/(asce)0733-9429(2008)134:4(378).

[16] Lu, Y., Chiew, Y. M., & Cheng, N. S. (2008). Review of seepage effects on turbulent open-channel flow and sediment entrainment. Journal of Hydraulic Research, 46(4), 476–488. doi:10.3826/jhr.2008.2942.

[17] Omar, P. J., Shivhare, N., Dwivedi, S. B., & Dikshit, P. K. S. (2022). Identification of soil erosion-prone zone utilizing geo-informatics techniques and WSPM model. Sustainable Water Resources Management, 8(3), 1–13. doi:10.1007/s40899-022-00654-9.

[18] Khan, M. A., Sharma, N., Pu, J. H., Pandey, M., & Azamathulla, H. (2022). Experimental observation of turbulent structure at region surrounding the mid-channel braid bar. Marine Georesources & Geotechnology, 40(4), 448–461. doi:10.1080/1064119X.2021.1906366.

[19] Ghonim, M. T., Jatwary, A., Mowafy, M. H., Zelenakova, M., Abd-Elhamid, H. F., Omara, H., & Eldeeb, H. M. (2024). Estimating the Peak Outflow and Maximum Erosion Rate during the Breach of Embankment Dam. Water (Switzerland), 16(3), 399. doi:10.3390/w16030399.

[20] Al-Riffai, M., & Nistor, I. (2010). Impact and analysis of geotechnical processes on earthfill dam breaching. Natural Hazards, 55(1), 15–27. doi:10.1007/s11069-010-9586-6.

[21] Urbaniak, M., Zamiar, K., & Kostecki, S. (2024). Understanding Geotechnical Embankment Washout Due to Overtopping: Insights from Physical Tests. Studia Geotechnica et Mechanica, 46(4), 328–336. doi:10.2478/sgem-2024-0025.

[22] Koshiba, T., Ono, S., Yamanoi, K., & Kawaike, K. (2024). Overtopping-induced levee breaches considering heterogeneous levee materials and outside flow. Hydrological Research Letters, 18(1), 22–27. doi:10.3178/hrl.18.22.

[23] Altomare, C., & Gironella, X. (2024). Characterization of Overtopping Volumes from Focused Wave Groups over Smooth Dikes with an Emerged Toe: Insights from Physical Model Tests. Journal of Marine Science and Engineering, 12(7), 1143. doi:10.3390/jmse12071143.

[24] van der Meer, J., Hardeman, B., Valk, J., Versteeg, S., Huis, M., Halter, W., ... & Mom, R. (2025). Improving Transitions At Grass Covered Dike Slopes Using the Wave Overtopping Simulator. Coastal Engineering Proceedings, 38(38), 22. doi:10.9753/icce.v38.papers.22.

[25] Pontillo, M., Schmocker, L., Greco, M., & Hager, W. H. (2010). 1D numerical evaluation of dike erosion due to overtopping. Journal of Hydraulic Research, 48(5), 573–582. doi:10.1080/00221686.2010.507005.

[26] Mares-Nasarre, P., Molines, J., Gómez-Martín, M. E., & Medina, J. R. (2021). Explicit Neural Network-derived formula for overtopping flow on mound breakwaters in depth-limited breaking wave conditions. Coastal Engineering, 164, 103810. doi:10.1016/j.coastaleng.2020.103810.

[27] Alqawasmeh, H. M. (2025). Simplified and Rapid Modeling of Road Embankments Slope Safety Factor Using Regularized Regression Techniques. Civil Engineering Journal, 11(9), 3873–3886. doi:10.28991/CEJ-2025-011-09-019.

[28] Gotoh, H., Ikari, H., Tanioka, H., & Yamamoto, K. (2008). Numerical Simulation of River-Embankment Erosion Due to Overflow by Particle Method. Proceedings of Hydraulic Engineering, 52, 979–984. doi:10.2208/prohe.52.979.

[29] Gupta, L. K., Pandey, M., & Raj, P. A. (2025). Numerical modeling of scour and erosion processes around spur dike. Clean - Soil, Air, Water, 53(3), 1–11. doi:10.1002/clen.202300135.

[30] Wu, H., & Zhao, K. (2025). Influence of soil porosity on hydraulic properties in dike failure induced by overtopping. Scientific Reports, 15(1), 16173. doi:10.1038/s41598-025-99699-x.

[31] Chen, W., Warmink, J. J., van Gent, M. R. A., & Hulscher, S. J. M. H. (2021). Numerical modelling of wave overtopping at dikes using OpenFOAM®. Coastal Engineering, 166(9), 103890. doi:10.1016/j.coastaleng.2021.103890.

[32] Hassan, M. A., & Mohamad Ismail, M. A. (2018). Effect of Soil Types on The Development of Matric Suction and Volumetric Water Content for Dike Embankment During Overtopping Tests. Civil Engineering Journal, 4(3), 668–688. doi:10.28991/cej-0309124.

[33] Prakoso, W. A., Hamdany, A. H., Wijaya, M., Ramadhan, R. I., Adinegara, A. W., Satyanaga, A., Adiguna, G. A., & Kim, J. (2025). Measurement of Soil–Water Characteristic Curve of Vegetative Soil Using Polymer-Based Tensiometer for Maintaining Environmental Sustainability. Sustainability (Switzerland), 17(1), 218. doi:10.3390/su17010218.

[34] Krisnanto, S., Rifdah, S. A., Ananda, A. A., & Putri, N. A. (2025). Analysis of the Stress State Variables for Unsaturated Soils with Compressible and Incompressible Soil Solids. International Journal of GEOMATE, 28(125), 92–100. doi:10.21660/2025.125.4734.

[35] Kang, Y.M., Yang, M.C., & Hu Y.X. (2006). Mixed Analysis on slope stability by limit equilibrium method and finite element method. China Mining Magazine, 15(3), 74-77. doi:10.3969/j.issn.1004-4051.2006.03.021.

[36] Duan, Z., Chen, J., Xie, J., Li, Q., Zhang, H., & Chen, C. (2024). Study on the Evolution Characteristics of Dam Failure Due to Flood Overtopping of Tailings Ponds. Water (Switzerland), 16(17), 2406. doi:10.3390/w16172406.

[37] Verwaest, T., Vanpoucke, P., Willems, M., & De Mulder, T. (2011). Waves Overtopping a Wide-Crested Dike. Coastal Engineering Proceedings, 1(32), 7. doi:10.9753/icce.v32.structures.7.